MAMA: an algebraic map for the secular dynamics of planetesimals in tight binary systems

A. M. Leiva,[1]★ J. A. Correa-Otto[1,2] and C. Beaugé[1,3]

[1]*Observatorio Astronómico, Universidad Nacional de Córdoba, Laprida 854, X5000BGR Córdoba, Argentina*
[2]*Instituto de Astronomia, Geofísica e Ciências Atmosféricas, USP, Rua do Matão 1226, 05508-900 São Paulo, Brazil*
[3]*Instituto de Astronomía Teórica y Experimental, Universidad Nacional de Córdoba, Laprida 854, X5000BGR Córdoba, Argentina*

ABSTRACT

We present an algebraic map (MAMA) for the dynamical and collisional evolution of a planetesimal swarm orbiting the main star of a tight binary system. The orbital evolution of each planetesimal is dictated by the secular perturbations of the secondary star and gas drag due to interactions with a protoplanetary disc. The gas disc is assumed eccentric with a constant precession rate. Gravitational interactions between the planetesimals are ignored. All bodies are assumed coplanar. A comparison with full *N*-body simulations shows that the map is of the order of 10^2 times faster, while preserving all the main characteristics of the full system. In a second part of the work, we apply multiparticle algebraic map for accretion (MAMA) to the γ-Cephei, searching for friendly scenarios that may explain the formation of the giant planet detected in this system. For low-mass protoplanetary discs, we find that a low-eccentricity static disc aligned with the binary yields impact velocities between planetesimals below the disruption threshold. All other scenarios appear hostile to planetary formation.

Key words: methods: analytical – celestial mechanics – planets and satellites: formation – stars: individual: γ-Cephei.

1 INTRODUCTION

Currently, there are more than 50 exoplanets detected in stellar binary systems (Chauvin et al. 2011). If the separation between the stellar components is larger than ∼50 au, the gravitational effects of the secondary star on a planetesimal or gas disc around the main star are small, and planetary formation is expected to proceed like in single stars. However, for compact (or tight) binary systems (hereafter, TBS), accretion can be seriously affected by the gravitational perturbations of the companion. Nevertheless, as many as five exoplanets are known to orbit individual components of TBS, the most extreme case being γ-Cephei, where the pericentric distance between the stellar components is only ∼12 au.

Many dynamical and collisional studies may be found in the literature trying to understand the process of planetary formation in TBS (e.g. Marzari & Scholl 2000; Thébault et al. 2004; Thébault, Marzari & Scholl 2006; Paardekooper, Thébault & Mellema 2008; Beaugé et al. 2010; Thébault 2011). So far, all attempts have been unsuccessful. The gravitational perturbations of the secondary star are too large and systematically lead to impact velocities beyond the disruption limit. Recently, Rafikov (2013) showed that the gravitational interaction with the gas disc could counteract the effects

of the binary, significantly reducing the collisional velocities of the swarm to acceptable levels. However, it appears that this requires a very massive discs, of the order of $0.1\,\mathrm{M_\odot}$. Since another effect of the binary is a severe truncation and mass-loss of the original protoplanetary disc (e.g. Artymowicz & Lubow 1994), it is not clear whether such massive discs would be expected in these systems.

Paardekooper et al. (2008) discussed that low collisional velocities could, in principle, be attained if the gas disc was permanently aligned with the binary and had an eccentricity similar to the forced eccentricities of the planetesimals. However, since at that time hydrosimulations showed precessing discs, this idea was not pursued. Recent years have shown a variety of hydrodynamical simulations of the dynamics of circumstellar gas discs in TBS (e.g. Kley & Nelson 2008; Kley, Papaloizou & Ogilvie 2008; Marzari et al. 2009, 2012; Müller & Kley 2012), adopting different thermodynamic properties and boundary conditions. While isothermic massless discs show moderate-to-high eccentricities ($e_\mathrm{g} \sim 0.1-0.2$) and relatively high retrograde precession rates ($|\varpi_\mathrm{g}| = |g_\mathrm{g}| \sim 2\pi/1000\,\mathrm{yr}^{-1}$), radiative discs and self-gravity seem to favour more circular and static discs (e.g. Marzari et al. 2012; Müller & Kley 2012). However, the results seem very sensitive to disc parameters, including the initial disc aspect ratio H/r and α-viscosity.

All previous simulations employed grid (i.e. Eulerian) codes, such as FARGO (Masset 2000) or RH2D (Kley 1999). Although Eulerian methods have proved very reliable for discs around single stars,
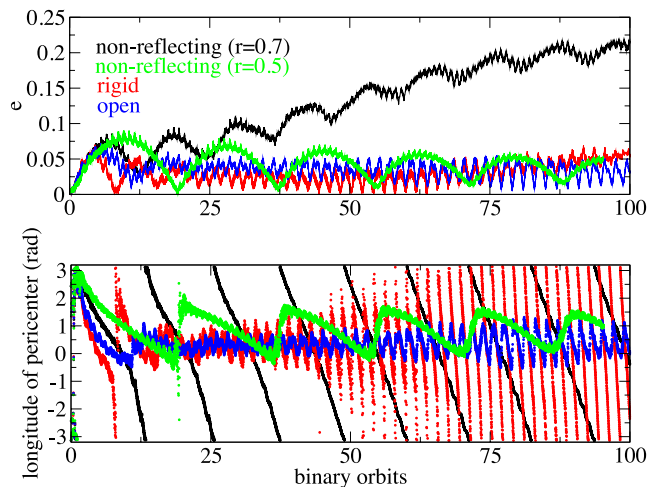
★ E-mail: mleiva@oac.uncor.edu

Figure 1. FARGO simulations of a circumstellar disc around γ-Cephei-A. Plots show the averaged gas eccentricity (e_g) and longitude of the pericentre ϖ_g as a function of time, for four different inner boundary conditions. For the first two runs, r is the inner radius of the disc.

there are some indications that they may be problematic for TBS. Fig. 1 shows four different FARGO simulations of a gas disc around γ-Cephei-A, perturbed by its binary companion. We chose masses and orbital elements following the best radial velocity fit by Hatzes et al. (2003). We adopted an initial $r^{-1/2}$ surface density profile with $\Sigma(r = 1) = 7 \times 10^{-4}$ g cm^{-2} an α-viscosity of $\alpha = 10^{-5}$. In all cases we chose an open outer boundary condition, but changed the inner boundary condition, as shown in the top left-hand corner of the upper plot. The resulting dynamics of the gas disc is very different, even far from the inner edge. In some cases the disc precesses, while in others the disc appears static. The behaviour of the eccentricity is also sensitive to the boundary condition, although perhaps in a lesser extent. Similar results were also found by Kley et al. (2008).

A different problem is related to the time-scale of the simulations. All predictions of the dynamics of protoplanetary discs are extrapolated from just $\sim 10^2$ orbital periods of the binary, even though many cases show evidence that the system has not yet reached an equilibrium. It may occur that secular perturbations from the binary would modify the results of the simulations, and these would only be noticeable in the long run. Since we expect planetary formation to take at least $\sim 10^5$ orbital periods of the binary, we wonder whether what we see in the short term is necessarily indicative of the long-term behaviour.

From these considerations, we believe that the real long-term equilibrium configuration of circumstellar discs in TBS is far from established. So, instead of adopting a given recipe for the gas dynamics and proving (or disproving) planetary formation in such a scenario, for the present paper we have chosen the inverse route. We will take the gas eccentricity and precession rate as variables in a parameter space, and search for those values that allow constructive collisions of a planetesimal swarm around the primary star of a TBS. Since this route implies a larger series of numerical simulations, we will present an algebraic map [dubbed multiparticle algebraic map for accretion (MAMA)] that facilitates this analysis. In particular, we will apply our map to γ-Cephei, a well-known and amply discussed system. Our results could guide future studies in disc dynamics trying to discover what thermodynamics properties they entail, or, conversely, if other planetary formation scenarios are required.

This manuscript is divided as follows: In Section 2, we review the differential equations governing the dynamics of small planetesimals affected by the gravitational perturbation of the stellar companion and the drag force from the gas. In Section 3, we construct the algebraic map (MAMA) for TBS, and compare its performance with respect to full N-body simulations. The application of MAMA to the γ-Cephei system is discussed in Section 4, where we search for disc parameters leading to accretion-friendly scenarios. Finally, conclusions close this work in Section 5.

2 DYNAMICS EVOLUTION OF SMALL PLANETESIMALS IN TBS

We begin assuming a TBS composed of a main star of mass m_A and a stellar companion of mass m_B. We choose a coordinate system centred in m_A with the z-axis parallel to the orbital angular momentum of the system. In this reference frame, we will denote by a_B the semimajor axis of the secondary, e_B its eccentricity and ϖ_B its longitude of pericentre (the origin of all longitudes is arbitrary).

We also assume that both the gas disc and the planetesimal disc orbit the primary star in the same plane. All orbital elements be m_A-centric. Our focus will then be on the dynamics of planetesimals when subject to gas drag and the gravitational perturbation of the secondary star.

A full study of this dynamics is a complicated task; however, it may be simplified considering a linear superposition of two interactions: (i) the drag gas with the disc (Weidenschilling et al. 1997; Supulver & Lin 2000; Beaugé et al. 2010) and (ii) the gravitational perturbation of the secondary (Heppenheimer 1978; Thébault et al. 2006; Giuppone et al. 2011). Each is discussed in the following sub-sections.

2.1 Gas drag

For spheric planetesimals with radius $s > 0.1$ km, the gas drag is a non-linear function of the relative velocity (v_{rel}) with respect to the gas, and its magnitude is proportional to v_{rel}^2 (Adachi, Hayashi & Nakazawa 1976; Weidenschilling et al. 1997; Supulver & Lin 2000). The acceleration suffered by the planetesimal is given by

$$\ddot{\boldsymbol{r}} = -\mathcal{C}|\boldsymbol{v}_{rel}|\boldsymbol{v}_{rel}, \tag{1}$$

where

$$\mathcal{C} = \frac{3C_D}{8}\frac{1}{s}\frac{\rho_g}{\rho_p}. \tag{2}$$

Here ρ_p and ρ_g are the volume densities of the planetesimal and gas, respectively, and $C_D = 0.44$ is a dimensional drag coefficient, usually considered constant for high Reynold numbers (Weidenschilling et al. 1997).

In a TBS, the gravitational perturbations of m_B cause drastic changes in the surface density of the gas disc. According to hydrosimulations (Paardekooper et al. 2008; Kley & Nelson 2008), the resulting surface density profile is almost linear up to an outer limit a_{out}, whose value is close to the location of the L_1 Lagrange point. Following Beaugé et al. (2010), we adopt a functional form for ρ_g given by

$$\rho_g(a) \simeq \frac{3}{2\pi}\frac{M_T}{a_{out}^3 H_R}\left(\frac{a_{out}}{a} - 1\right), \tag{3}$$

where M_T is the total mass of the disc, $H_R = 0.05$ is its scaleheight, and a the semimajor axis of each gas element. For γ-Cephei, we find that $a_{out} \simeq 5$ au.

The gas disc has a negative pressure gradient which causes it to orbit m_A with a sub-Keplerian velocity: $\boldsymbol{v}_g = \alpha \boldsymbol{v}_{\mathrm{Kep}}$. Following Adachi et al. (1976), we assume $\alpha = 0.995$. Then, the relative velocity between a planetesimal and a gas element, both at a given position $\boldsymbol{r}$, is given in polar coordinates by $\boldsymbol{v}_{\mathrm{rel}} = v_r \hat{r} + v_\theta \hat{\theta}$, where

$$v_r = \sqrt{\frac{\mu}{p}} \left[e \sin(f) - \alpha \, e_g \sin(f + \Delta\varpi) \cdot \right.$$

$$\left. \cdot \left(\frac{1 + e \cos(f)}{1 + e_g \cos(f + \Delta\varpi)} \right)^{\frac{1}{2}} \right]$$

$$v_\theta = \sqrt{\frac{\mu}{p}} \left[(1 + e \cos f) - \alpha \left(1 + e_g \cos(f + \Delta\varpi) \right) \cdot \right.$$

$$\left. \cdot \left(\frac{1 + e \cos(f)}{1 + e_g \cos(f + \Delta\varpi)} \right)^{\frac{1}{2}} \right]. \tag{4}$$

In these expressions, a, e, ϖ and f are the semimajor axis, eccentricity, longitude of pericentre and true anomaly of the planetesimal, $\Delta\varpi = \varpi - \varpi_g$, $\mu = \mathcal{G}m_A$, $\mathcal{G}$ the gravitational constant and $p = a(1 - e^2)$ the semilactus rectum. The reader is referred to Beaugé et al. (2010) for more details.

The variational equations for the reduced set of variables (a, e, ϖ) can be obtained from Gauss' perturbation equations (e.g. Roy 2005):

$$\left. \frac{da}{dt} \right|_{\mathrm{drag}} = \frac{2a^2}{\sqrt{\mu p}} \left(R' \, e \sin f + T' \, (1 + e \cos f) \right)$$

$$\left. \frac{dk}{dt} \right|_{\mathrm{drag}} = \sqrt{\frac{p}{\mu}} \left(R' \, \sin(f + \varpi) \right.$$

$$\left. + T' \, \frac{(2 + e \cos f) \cos(f + \varpi) + e \cos \varpi}{1 + e \cos f} \right)$$

$$\left. \frac{dh}{dt} \right|_{\mathrm{drag}} = \sqrt{\frac{p}{\mu}} \left(- R' \, \cos(f + \varpi) \right.$$

$$\left. + T' \, \frac{(2 + e \cos f) \sin(f + \varpi) + e \sin \varpi}{1 + e \cos f} \right), \tag{5}$$

where $(k, h) = (e \cos \varpi, \, e \sin \varpi)$ are the Cartesian analogues of (e, ϖ). Functions R' and T' are the radial and transverse component of the acceleration due to the gas drag and are defined by $R' = -\mathcal{C}|\boldsymbol{v}_{\mathrm{rel}}| \, v_r$ and $T' = -\mathcal{C}|\boldsymbol{v}_{\mathrm{rel}}| \, v_\theta$.

2.2 Secular gravitational perturbations

Our study is performed in the restricted three-body problem. This implies that we will disregard the perturbations of the planetesimals and gas on m_B, which will move in a fixed elliptical orbit around the main star. Also, we will neglect the mutual gravitational interactions between the planetesimals themselves.

In this scenario, and outside any significant mean-motion resonances (MMRs) between the planetesimals m and m_B, the gravitational dynamics of the small bodies will be dominated by secular perturbations, as well as short-period terms associated with the mean longitudes. These latter contributions can be eliminated by a perturbation technique known as averaging, in which the osculating variables (a, k, h, f) and transformed to averaged variables (a^*, k^*, h^*, f^*) which do not contain the short-period variations. In the av-

eraged (secular) system, the 'proper' semimajor axis a^* is constant and the only pertinent variables are (k^*, h^*). The resulting equations of motion are then

$$\frac{dk^*}{dt} = -gh^*; \quad \frac{dh^*}{dt} = g(k^* - e_f), \tag{6}$$

where g is the secular frequency and e_f is the forced eccentricity. Using a second-order Hori-type averaging procedure, Giuppone et al. (2011) found approximate expressions for both quantities:

$$g = \frac{3}{4} \frac{m_B}{m_A} \frac{n^* a^{*3}}{a_B^3 \left(1 - e_B^2\right)^{3/2}} \left[1 + 32 \left(\frac{m_B}{m_A} \right) \left(\frac{a^*}{a_B} \right)^2 \left(1 - e_B^2\right)^{-5} \right],$$

$$e_f = \frac{5}{4} \frac{a^*}{a_B} \frac{e_B}{\left(1 - e_B^2\right)} \left[1 - 16 \left(\frac{m_B}{m_A} \right) \left(\frac{a^*}{a_B} \right)^2 \left(1 - e_B^2\right)^{-5} \right], \tag{7}$$

where n^* is the proper mean motion. The terms within the square brackets are the second-order contributions and do not appear in first-order theories such as Heppenheimer (1978). The reader is referred to Giuppone et al. (2011) for a comparison between both secular models.

The secular system (6) is linear and can be easily solved analytically. Given initial conditions (a_0^*, k_0^*, h_0^*), we can write

$$a^*(t) = a_0^*$$

$$k^*(t) = e_p \cos(g \, (t - t_0) + \phi_0) + e_f$$

$$h^*(t) = e_p \sin(g \, (t - t_0) + \phi_0), \tag{8}$$

where t_0 is the initial time, $e_p^2 = (k_0^* - e_f)^2 + (h_0^*)^2$ and $\tan \phi_0 = h_0^*/(k_0^* - e_f)$. The quantity e_p is sometimes referred to as the free eccentricity.

2.3 Linear superposition of the two interactions

Our complete model will be the direct sum of equations (5) and (6). However, it must be noted that the secular model (6) was constructed with the averaged orbital elements while the drag model (5) assumes osculating elements. Even so, since a exhibits periodic variations around a^*, a more precise reproduction of the orbital decay from gas drag will be obtained if we adopt a^* instead of a in equations (5).

To merge both sets of differential equations, we must find a relation between osculating and proper variables. Instead of employing cumbersome canonical transformations (e.g. Giuppone et al. 2011), in this paper we preferred a purely numerical approach.

Preliminary tests showed that the difference between (k^*, h^*) and (k, h) is not significant to the overall evolution of the system. Since our aim is to keep the complete model as simple as possible, we opted for neglecting the transformation of the secular variables. As we will show below, this approximation is good enough to our purposes. The difference between a and a^*, on the other hand, are mainly noticeable in the orbital decay time-scale. Although the errors introduced by neglecting the transformation $a \to a^*$ are not large (of the order of $\sim$1–5 per cent), they are easily remedied.

The functional form $a^*(a)$ was built numerically. First, we performed N-body simulations for the dynamical evolution of the semimajor axis of several test particles, each with a different initial value $a_0 \in [1, 5]$ au, $e_0 = 0$ and mean anomaly $M_0 = 0°$. The initial value of e is not important, since the most important term in the amplitude of a is of the order of zero in the eccentricity.

In all cases, we adopted the γ-Cephei binary system. The output $a(t)$ of each simulation was then transformed to a^* using a low-pass finite impulse response filter (e.g. Carpino, Milani & Nobili
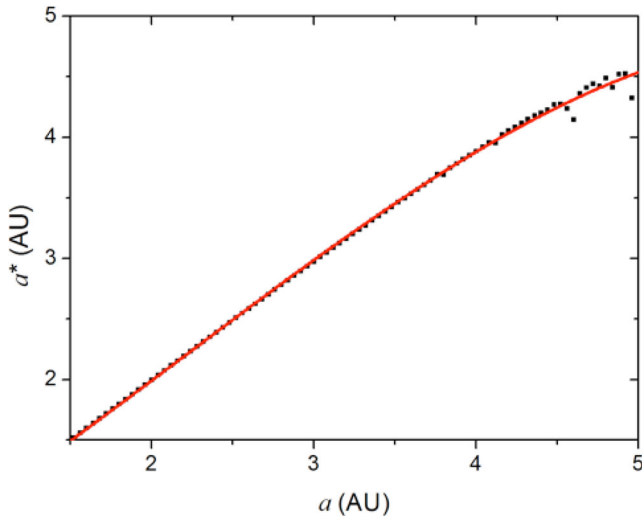
Figure 2. Relation between the osculating (*a*) and proper (*a**) semimajor axis, the black dots show numerical results, while the red curve corresponds to the empirical fit (9).

1987) designed to remove all periodic variations up to five orbital periods of the binary. The resulting distribution of a^* for each initial osculating a_0 is plotted in Fig. 2 (black circles). The red curve shows a numerical fit using a cubic polynomial in a, whose expression is

$$a^* = 0.219\,59 + 0.673\,50a + 0.149\,75a^2 - 0.022\,37a^3. \qquad (9)$$

The agreement with the numerical results is very good. However, it is important to keep in mind that this polynomial is only valid for initial conditions with $M_0 = 0$. Thus, in all numerical simulations performed in this work we will adopt the same initial mean anomaly for the particles.

With the empirical relation (9) between the osculating and proper semimajor axis, we can construct the complete model. Then, with the linear superposition of the models (5) and (6) we obtain the complete dynamical model as

$$\frac{\mathrm{d}a}{\mathrm{d}t} = \left.\frac{\mathrm{d}a}{\mathrm{d}t}\right|_{\mathrm{drag}}$$

$$\frac{\mathrm{d}k}{\mathrm{d}t} = \left.\frac{\mathrm{d}k}{\mathrm{d}t}\right|_{\mathrm{drag}} - g\,h$$

$$\frac{\mathrm{d}h}{\mathrm{d}t} = \left.\frac{\mathrm{d}h}{\mathrm{d}t}\right|_{\mathrm{drag}} + g\,(k - e_{\mathrm{f}}), \qquad (10)$$

where the drag terms in the two latter equations must also be evaluated at a using its relationship with a^*.

2.4 Comparison between *N*-body simulations and the secular model

To test the accuracy of the model, we chose once again the γ-Cephei system as our working example. We first performed a series of *N*-body simulations of the evolution of the planetesimals with different physical radii and initial conditions, and then compared the results with numerical integrations of equations (10). In both cases, the differential equations were solved with a Bulirsch–Stoer code using an accuracy of 10^{-11}.

Figs 3 and 4 show two extremes cases. Plots on the left correspond to planetesimals with radii $s = 1$ km, while those on the right to $s = 50$ km, both assuming $\rho_{\mathrm{p}} = 3$ g cm^{-3}. In Fig. 3, the initial
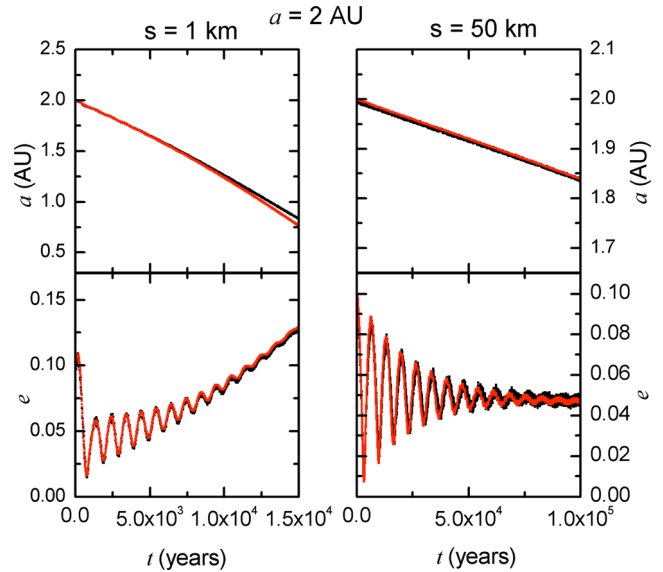

Figure 3. Temporal evolution of a and e for two different size planetesimals, $s = 1$ km (left) and $s = 50$ km (right). Initial osculating semimajor axis was chosen equal to $a_0 = 2$ au. The black dots show the results of the full *N*-body numerical simulation, while the red curves correspond to model (10).
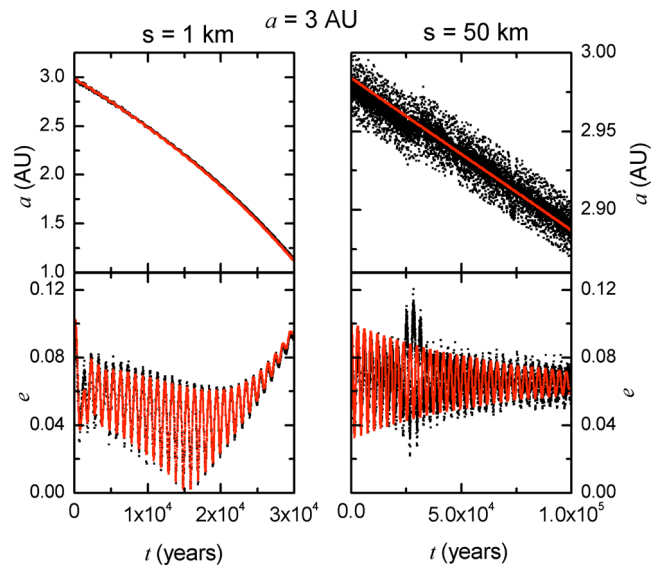

Figure 4. Same as previous figure, but now the initial osculating semimajor axis was $a_0 = 3$ au.

osculating semimajor axis was chosen equal to $a_0 = 2$ au, while in Fig. 4 this value was increased to $a_0 = 3$ au. Other orbital elements were $M = 0°$, $e_0 = 0.1$ and $\varpi_0 = 0°$. We assumed an eccentric gas disc ($e_{\mathrm{g}} = 0.2$) with a retrograde precession rate equal to $2\pi/|g_{\mathrm{g}}| = 1000$ yr. The disc was further assumed to have a volume density of $\rho_{\mathrm{g}}(2\,\mathrm{au}) = 5 \times 10^{-10}$ g cm^{-3} (Paardekooper et al. 2008; Beaugé et al. 2010) and an outer truncation radius $a_{\mathrm{out}} = 5$ au.

From these results, we can see that the dynamical behaviour of small planetesimals ($s = 1$ km, left-hand panels) is well reproduced by our model. For these bodies, the interaction with the gas disc is dominant over the gravitational perturbations from the binary. The simple averaged equations give a correct qualitative (and quantitative) prediction about the orbital decay, as well as the amplitude, frequency and damping of the eccentricity.

For large planetesimals ($s = 50$ km, right-hand panels), on the other hand, the gravitational perturbations from m_B are more important than the drag gas. For the planetesimal of initial semimajor axis $a_0 = 2$ au (Fig. 3), the model gives a very good approximation to the real dynamics. The same agreement is also observed for larger initial semimajor axis ($a_0 = 3$ au, Fig. 4), although our model fails to reproduce an excitation in the eccentricity and a temporary jump in the semimajor axis, both occurring simultaneously at $t \sim 2.5 \times 10^4$ yr. A closer look reveals that this behaviour is generated by a passage through a high-order MMR with the binary (see Giuppone et al. 2011 for more detailed examples). Since resonant interactions are not included in our model, equations (10) are unable to reproduce this effect. Nevertheless, with the exception of the resonance scattering, the results of the model seem very accurate.

3 HIGH-ORDER MEAN-MOTION RESONANCES IN THE γ-CEPHEI SYSTEM

Since the outer parts of both the gas and planetesimal discs may lie in regions affected by MMR, they could seriously impair the use of our secular model. Thus, before proceeding in the construction of our algebraic map, it is important to evaluate the effects of high-order commensurabilities in the possible accretion process. Our first analysis along these lines will be to map the regions of regular and chaotic motion for a wide range of initial conditions. As before, we adopt γ-Cephei as our working example.

We considered a grid of 3000×201 initial conditions in the semimajor axis versus eccentricity plane, with values in the intervals $a \in [2, 5]$ au and $e \in [0.0, 0.2]$. The number of points in each axis correspond to an equal step of $\Delta a = 0.001$ au and $\Delta e = 0.001$ between successive points. Starting values for the angles where taken equal to zero, except for $\lambda = M + \varpi$ which has taken equal to $180°$. All the test particles were integrated for 2×10^5 yr (equal to ~ 3500 orbital periods of the binary) using an N-body code with a Bulirsch–Stoer integrator (precision $ll = 10^{-12}$).

For each orbit, we calculated the averaged mean exponential growth factor of nearby orbits (MEGNO) indicator $\langle Y \rangle$ (Cincotta & Simó 2000). This quantity has proven to be an efficient identifier of chaotic behaviour, been significantly faster than the classical maximum Lyapunov exponent. Recall that values $\langle Y \rangle \leq 2$ correspond to regular orbits, while $\langle Y \rangle > 2$ are indicative of chaotic motion.

Results are shown in Fig. 5, where the colour associated with each initial conditions is related to the final value of $\langle Y \rangle$. Regular orbits are shown in light grey, while chaotic solutions are shown in black. The top plot presents the complete map, while the bottom graph zooms in on the interval between 3.4 and 4.4 au.

For $a < 4$ au, most of the phase plane is dominated by regular orbits, crossed by thin almost-vertical stripes of chaotic motion, each associated with a different MMR. This far from the perturber, the resonances are isolated and their effect is restricted to a small region around their centre. Conversely, the outer region of the map beyond 4 au is almost completely chaotic, with only small areas of regular motion at low eccentricities. In this region, the libration width of the MMRs are sufficiently large to allow overlap even for moderate eccentricities and, thus, cause the appearance of zones characterized by global chaos. Finally, for $a > 4.5$ au the resonance overlap is complete even for quasi-circular orbits, and all initial conditions are dynamically unstable. Note how the outer limit of the gas disc in this system (located near 5 au, according to hydrodynamical simulations) shows a good agreement with the region of the phase plane immersed in a chaotic sea even for circular orbits.
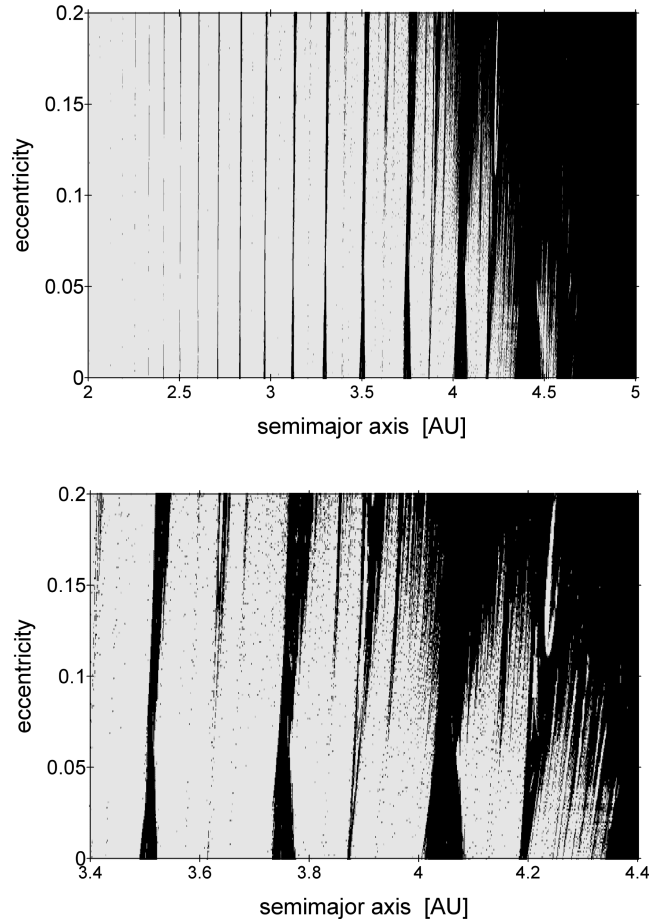

Figure 5. MEGNO map of 3000×201 initial conditions in the a–e plane, each corresponding to test-particles in the γ-Cephei binary system. Total integration time was equal to 2×10^5 yr. Light grey dots indicate regular orbits, while black dots correspond to chaotic solutions.

To estimate which MMR are associated with each chaotic zone, we can calculate its position from Kepler's third law. Given a generic $(p + q)/p$ commensurability, the nominal (i.e. exact) resonant semimajor axis is given by

$$a = a_B \left(\frac{m_A}{m_A + m_B} \right)^{1/3} \left(\frac{p}{p+q} \right)^{2/3}. \quad (11)$$

Table 1 shows the nominal position of several first-degree resonances in the region of interest. Here, we have adopted the classical nomenclature in which the value of q gives the *order* of the commensurability, while p is its *degree*. A comparison between these positions and the dynamics maps in Fig. 5 shows two important results.

First, all the stripes of strong chaotic motion in the top panel are associated with first-degree MMR of high order. In Solar system problems, high-order resonances have negligible dynamical consequences, but in the present system the combination of a large mass and high-eccentricity perturber enhances their effects. Later on we will analyse just how important they can be in the dynamical evolution of test planetesimals. Thinner stripes, specially noticeable in the lower plot, correspond to second and third-degree resonances. The region $a > 4$ au is specially rich in these structures forming a forest of lines that contribute to the resonance overlap.

A second result is that the locations of the resonances are significantly shifted with respect to the exact semimajor axes. This is

Table 1. Nominal semimajor axis of several first-degree MMR in the γ-Cephei system.

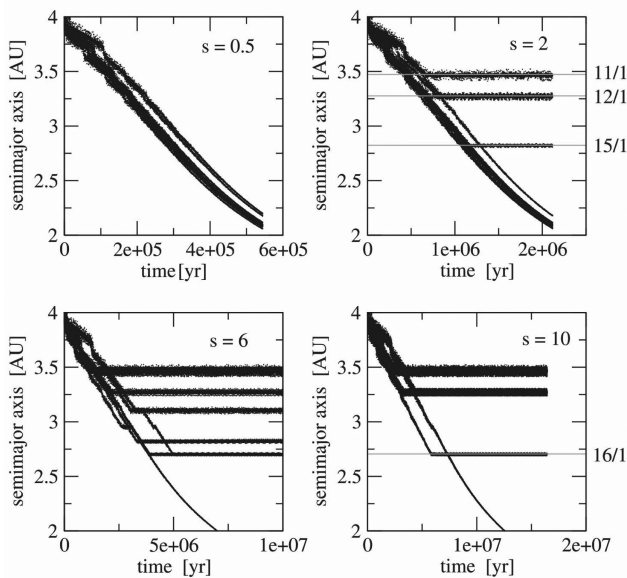| $(p+q)/p$	a (au)
8/1	4.300
9/1	3.970
10/1	3.700
11/1	3.472
12/1	3.276
13/1	3.106
14/1	2.956
15/1	2.823
16/1	2.705
17/1	2.597
18/1	2.500

Figure 6. *N*-body simulations of planetesimals in the γ-Cephei system, under the combined effects of gravitational perturbations and gas drag. Each panel shows the semimajor axis, as function of time, of a set of 10 fictitious bodies with $a_0 = 4$ au, $e_0 = 0.1$ and random initial mean anomalies. The radii s of the planetesimals are indicated (in km) in the top right-hand corner of each plot. The location of the strongest MMR are shown in both right-hand graphs.

expected from what is sometimes known as the 'Law of Structure' (Ferraz-Mello 1988) or the 'pericentric branch' (e.g. Moons & Morbidelli 1993). Basically, this means that the centre of the resonance domain is a function of the eccentricity, and is usually shifted away from the exact semimajor axis. The magnitude of this shift is very sensitive with respect to the system parameters, particularly m_B and e_B.

While Fig. 5 appears to indicate limited effect of MMRs on planetesimal orbits with $a < 4$ au, these dynamical maps correspond to the conservative problem in which the effects of the gas drag are not considered. Fig. 6, on the other hand, shows the evolution of the semimajor axis of four different sets of 10 fictitious planetesimals, again in the γ-Cephei system, with a non-linear drag. Initial conditions were chosen equal to $a_0 = 4$ au, $e_0 = 0.1$, $\Delta\varpi = \varpi - \varpi_B = 0$ and random values of the mean anomaly M_0. The gas

disc was assumed static (no precession) and with a small eccentricity ($e_g = 0.05$). In the top left-hand panel, we considered small planetesimals with physical radii $s = 0.5$ km, while for the bottom right-hand plot we used $s = 10$ km. Other plots correspond to intermediate values.

Giuppone et al. (2011) showed that some planetesimals could undergo resonance trapping, even though the effects of the drag leads to divergent migration. Here, we can see the same effect in more detail, and how it varies according to the size of the planetesimal. For very small bodies the orbital decay is very pronounced and cannot be overcome by the resonant perturbations; consequently no resonance trapping is observed and all passages are characterized by temporary excitations of the eccentricity. In a little over 5×10^5 yr all the planetesimals have already fallen below the semimajor axis of the observed planet (i.e. ~ 2 au), and the overall dynamical evolution is primarily dictated by gas drag and secular gravitational effects.

For larger bodies, the time-scale for orbital decay is longer than the typical libration period within the MMR. Resonance trapping is now possible, even though the commensurabilities are of high order. For $s = 2$ km, only ~ 30 per cent of the bodies are trapped, while this number increases to about ~ 90 per cent for $s = 10$ km. The 11/1 MMR is the preferred location, although some trapping is also observed in other commensurabilities down to the 16/1. However, for $s > 6$ km the orbital decay towards the resonance already takes longer than the expected timespan of the gas disc, so it is questionable whether this effect would be dynamically significant in real systems.

These simulations were performed for a static gas disc. As shown by Beaugé et al. (2010), a precessing disc causes a faster orbital decay, so resonance trapping is less effective in those cases. Simulations using a retrograde precession rate of $g_g = -2\pi/1000 \, \text{yr}^{-1}$ show that resonance trapping is ineffective for $s < 50$ km.

In conclusion, we have found that resonant effects should be important in the dynamical evolution of relatively large planetesimals with initial semimajor axis $a > 3$ au, especially in static gas discs. In those cases our secular model should be used with caution. However, for initial conditions closer to the star, MMR seem to be of little consequence, and our model described by equations (10) can constitute a working and adequate approximation to the real dynamics.

4 THE ALGEBRAIC MAP MAMA

Although our mixed-secular model (10) is much faster than a full *N*-body simulation of the exact equations, we can drastically improve its performance by the implementation of an algebraic map. This is desirable if we want to test many different system parameters, searching for the most friendly scenario for the process of accretion.

Following the pioneering works of Malhotra (1994), Cordeiro, Canova & Vieira Martins (1997) and Mikkola (1997), we can construct our algebraic map as an extension of the classical leap-frog algorithm for dissipative systems. We begin by rewriting the complete analytical model as

$$\frac{da}{dt} = \left.\frac{da}{dt}\right|_{\text{grav}} + \left.\frac{da}{dt}\right|_{\text{drag}}$$

$$\frac{dk}{dt} = \left.\frac{dk}{dt}\right|_{\text{grav}} + \left.\frac{dk}{dt}\right|_{\text{drag}}$$

$$\frac{dh}{dt} = \left.\frac{dh}{dt}\right|_{\text{grav}} + \left.\frac{dh}{dt}\right|_{\text{drag}}, \qquad (12)$$

where the first term of the r.h.s. is the gravitational contribution from the binary, for which $\frac{da}{dt}|_{grav} \equiv 0$. While the gravitational terms define an autonomous system, the drag terms include the time implicitly through the true anomaly f.

Defining Δt as the time-step, the algebraic map is constructed by the following sequence of steps.

(i) Step 1 (Drift): $(a_0^*, k_0, h_0, M_0) \rightarrow (a_1^*, k_1, h_1, M_1)$.
Given initial conditions (a_0^*, k_0, h_0, M_0), where M_0 is the mean anomaly at $t = t_0$, we integrate system (12) considering only the conservative terms for half a time-step $\Delta t/2$. Since this 'unperturbed' system has an analytical solution in closed form, we simply obtain:

$$a_1^* = a_0^*$$

$$k_1 = e_p \cos{(g\,\Delta t/2 + \phi_0)} + e_f$$

$$h_1 = e_p \sin{(g\,\Delta t/2 + \phi_0)}, \tag{13}$$

where the values of e_p, e_f and g are calculated at a_0^*. The mean anomaly is estimated with $M_1 = n_0^* \Delta t/2 + M_0$. This is obviously an approximation, since we are considering the mean-motion n_0^* instead of its osculating value, but test simulations (see Figs 3 and 4) show the error is not significant.

(ii) Step 2 (Kick): $(a_1^*, k_1, h_1, M_1) \rightarrow (a_2^*, k_2, h_2, M_2)$.
We now apply a first-order integration, applying solely the drag effects, for a time-step Δt

$$a_2^* = a_1^* + \Delta T \left.\frac{da^*}{dt}\right|_{drag}$$

$$k_2 = k_1 + \Delta T \left.\frac{dk}{dt}\right|_{drag}$$

$$h_2 = h_1 + \Delta T \left.\frac{dh}{dt}\right|_{drag}, \tag{14}$$

where the value of the true anomaly f_1 in the drag equations is determined from the mean anomaly M_1 solving Kepler's equation. The mean anomaly M_2 is left unchanged, so that $M_2 = M_1$.

(iii) Step 3 (Drift): $(a_2^*, k_2, h_2, M_2) \rightarrow (a_3^*, k_3, h_3, M_3)$.
Finally, we repeat Step 1 for a time-step $\Delta t/2$, updating the initial conditions and values of e_p, e_f and g according to the new proper semimajor axis.

As usual, after the first application of the map, both drifts can be fused into a single application of the conservative equations for a full time-step interval Δt. This scheme defines our algebraic map for the complete model, hereafter referred to as MAMA.

4.1 Step time for MAMA

In order to apply MAMA successfully, we must specify a value for the time-step Δt that guarantees a fast code with accurate results. Once again, we considered the γ-Cephei system as an example, and assumed an eliptical disc ($e_g = 0.1$) around the main star m_A. We then analysed the dynamical evolution of five different planetesimals ($s = 1, 5, 10, 20$ and 50 km), comparing the full numerical solutions of the complete model (10) with the application of the algebraic map. Both integration methods were followed for 10^3 yr, at the end of which we calculated the relative difference in semimajor axis and eccentricity (denoted by er_A and er_E, respectively).

Results are shown in Fig. 7 for initial semimajor axis $a_0 = 2$ au, where there is an evident increase in the error for smaller value of s,
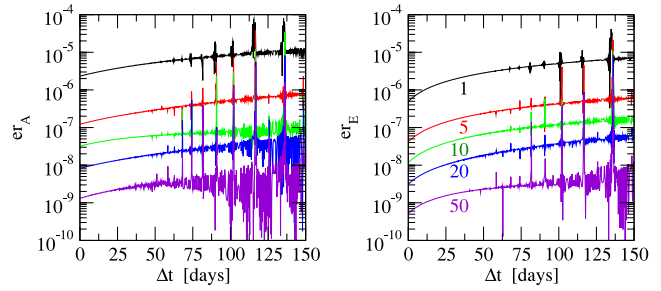

Figure 7. Maximum relative errors for the semimajor axis (er_A) and the eccentricity (er_E) as function of the step time of MAMA, and for planetesimals of different size. Black: $s = 1$, red: $s = 5$, green: $s = 10$, blue: $s = 20$, violet: $s = 50$, where all values are given in kilometres.
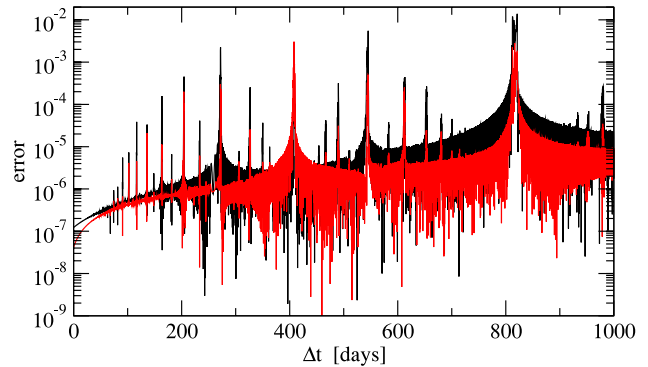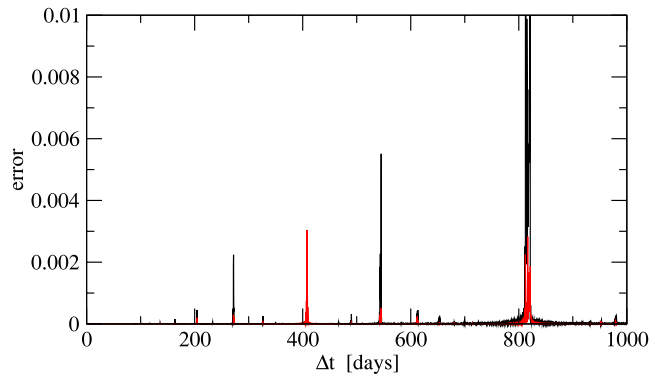

Figure 8. Maximum relative errors for the semimajor axis (black) and the eccentricity (red) as function of the step time of MAMA, for a planetesimal of radius $s = 5$ km. Top frame shows results in linear scale, while the bottom plot shows the same results in log-scale. Note the appearance of peaks when the time step Δt is commensurate with the orbital period of the planetesimal $T \simeq 820$ d.

for which the drag term is more important. Although for small values of Δt, the error is linear with the step size (as expected from a leap-frog-based map), we also note the appearance of localized peaks in the errors, that occur for the same values of Δt independently of the particle size.

Fig. 8 shows the same behaviour in more detail, where we compared MAMA and full N-body integrations for a single planetesimal with $a_0 = 2$ au and $s = 5$ km. Here the time-step interval was extended up to 1000 d, larger than the orbital period of the particle $T \simeq 820$ d. We can see that the peaks appear precisely at values commensurate with the T. The largest occurs at a 1:1 resonance (i.e. $\Delta t/T = 1/1$), while others are also visible at ratios equal to 2:3, 1:2, 1:3 and 1:4. This effect seems to be a consequence of the

passage from the original ordinary differential equation to discrete equations which contain an implicit dependence on time in the form of delta functions.

Since these commensurabilities are an artefact of the algebraic mapping and affect the overall precision of the results, they must be avoided whenever possible. We have therefore adopted a value equal to $\Delta t = 150$ d. Although some peaks are still visible in this range (see Fig. 7), their amplitudes are not very significant and the maximum error in both eccentricity and semimajor axis always seem to be below 10^{-4}, even for planetesimals with very small radii. It should be stressed, however, that this step size is recommended for a TBS with masses and orbital elements corresponding to γ-Cephei. If MAMA were to be applied to another binary system, similar tests as those described here should be performed to estimate the best time-step.

4.2 Sample test

To test MAMA under these conditions, we considered a total sample of 10^5 initial conditions in circular orbits distributed uniformly between 1 and 4 au, and adopting random values for the mean anomalies. These were separated into 10 different values of the particle size, between $s = 1$ and $s = 10$ km, considering 10^4 initial conditions for each radius. Each was then evolved using our map under the gravitational effects of the secondary star of γ-Cephei plus gas drag. For the gas, we assumed an axisymmetric gas disc ($e_g = 0$, $g_g = 0$) with the same characteristics as described in Section 2.4 ($a_{out} = 5$ au and $\rho_g = 5 \times 10^{-10}$ g cm^{-3} at $a = 2$ au).

The results are shown in Fig. 9, were we plot the variation of the eccentricities after 100 binary orbits. Colours identify different particle sizes. For comparison, we also plotted in broad black curves the evolution of the same initial conditions without the effects of gas drag.

In accordance with the secular equations (6) and (7), the particles exhibit an oscillation in eccentricity from 0 to $2e_{fG}$ with a secular frequency g_G that is a function of the semimajor axis. Gas drag causes a systematic damping of the amplitude of oscillation (e.g. Marzari & Schooll 2000). Thus, the smallest particles show a smaller amplitude of oscillation than their bigger companions. The
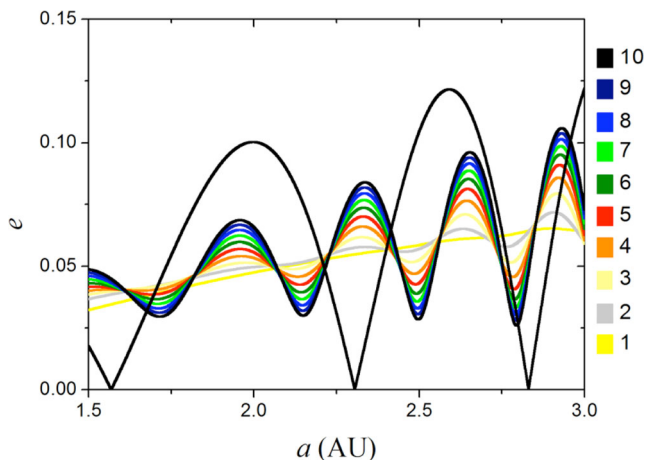

Figure 9. Eccentricity as function of the semimajor axis, at $t = 100$ binary orbits, of an initial swarm of 10^5 the particles. The broad black line shows results of the conservative secular model, while other curves correspond to simulations with a non-linear gas drag. All orbital configurations were evolved using MAMA and show excellent agreement with a full N-body simulation.
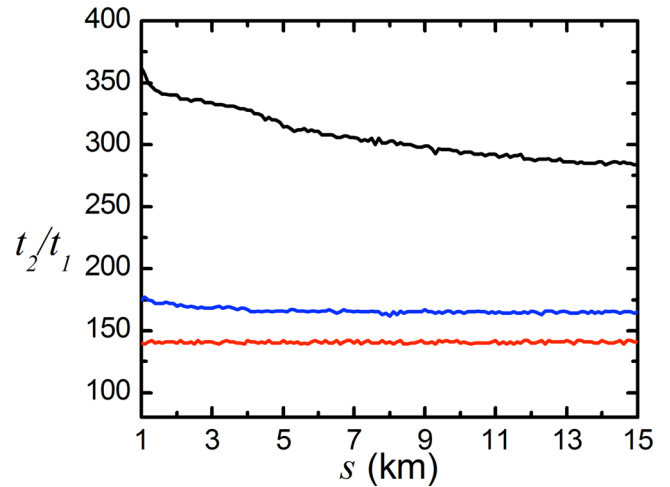

Figure 10. Ratio of the average computation time between the numerical integrator (t_2) and MAMA (t_1), for planetesimals of different sizes. The particles start with three different values of the semimajor axis: 1 au (black), 2 au (blue) and 4 au (red).

results obtained with MAMA are in excellent agreement with those presented by other authors (e.g. Thébault et al. 2006; Paardekooper & Leinhardt 2010).

4.3 Speed of MAMA

Having computed an adequate time-step, and checked its precision, now we turn to the CPU effectiveness of MAMA when compared with a full N-body numerical simulation. Once again we chose the γ-Cephei system as example, with an m_A-centric eccentric precessing gas disc with $e_g = 0.2$ and $g_g = -2\pi/1000$ yr^{-1}. For this test, we considered a set of 140 planetesimals with radii between 1 and 15 km, which are integrated for a total timespan of 2000 yr.

To solve the exact equations, we used a Bulirsch–Stoer integrator with an adaptive step size, and an error tolerance of $ll = -12$. We carried out three different tests. In all cases, initial conditions were chosen with $e = 0$, $M = 0$, but with different semimajor axis: 1, 2 and 4 au. We then average the CPU time for the different size particles and we estimated an averaged time t_2 for each set. Finally, we compare these values with those obtained employing MAMA and denoted these values as t_1. The resulting ratio t_2/t_1 is shown in Fig. 10, where each set is plotted using a different colour: black (1 au), blue (2 au) and red (4 au). We can see from that MAMA is systematically much faster than the N-body code, although the exact rate depends on the semimajor axis. Even so, the algebraic map is (at worse) 100 times faster than a full integration of the exact equations of motion.

5 ACCRETIONAL CONDITIONS IN THE γ-CEPHEI SYSTEM

As discussed in the introduction, the problem of planetesimal accretion in TBS is extremely complex. Although in part this is due to uncertainties in the structure and dynamics of their primordial gaseous discs, it is also affected by our lack of knowledge of the behaviour of planetesimal swarms under different disc structures. While the first of these problems are beyond the scope of this work, we may employ MAMA as a working bench to attempt to gain insight on how different disc scenarios may affect collisional velocities and possible accretion among small-size planetesimals.

With these considerations in mind, and for a sake of simplicity, in this section we consider a static (non-precessing) disc with its pericentre aligned with the pericentre of the orbit of the secondary star ($\varpi_g = \varpi_B = 0$). Then, the only free parameter we need to consider is the eccentricity (e_g) of the disc. We could have chosen to examine the role of any other parameter, but the ellipticity of the gas component is probably the most sensitive one affecting the orbital evolution of small solid bodies.

We analysed the role of e_g considering fixed values between 0.025 and 0.2 with steps of $\Delta e_g = 0.025$. For each value, we generated a total of 16 000 initial conditions for the planetesimals. Their initial semimajor axis were chosen in the interval $1-4$ au and their radii between 1 and 10 km. This defined a grid in the (a, s) plane with spacing $\Delta a = 0.1$ au and $\Delta s = 0.025$ km. All initial orbits were circular with random values of the mean anomaly.

The secular phase space of planetesimals embedded in a circumstellar disc in a TBS has a stable equilibrium solution. For a static disc, this solution is a fixed point in the (k, h) plane (Paardekooper et al. 2008; Beaugé et al. 2010), while for a precessing disc the stationary orbits are limit cycles (Beaugé et al. 2010). The orbital evolution was followed for 3×10^5 yr, after which all planetesimals reached their equilibrium solutions. Their final values of the eccentricity e and longitude of pericentre ϖ, as function of their initial semimajor axis, are shown in Figs 11 and 12; the first for discs with $e_g \leq 0.1$, while the second presents results for higher values. The different 'curves' are actually sequences of points made up of planetesimals of equal sizes. While in most cases a size spectrum leads to a significant spread in final values of the secular variables, for values of $e_g \sim 0.05$ the solutions appear more coherent.

An advantage of our map is that it keeps track of the true longitude of all particles, thus allowing for the identification of possible collisions. We then proceeded to calculate the impact velocities between planetesimal pairs for each value of e_g. The best results are shown in Fig. 13, were we plotted the average relative velocities as function of the semimajor axis. The left-hand plot, corresponding to a disc with $e_g \sim 0.05$ shows the most promising scenario, in which most collisions between particles with $a \in [2, 3.7]$ au led to values below 50 m s^{-1}. A slightly higher eccentricity for disc, however, leads to a much smaller accretion-friendly region, now restricted to values close to 3 au.

From Stewart & Leinhardt (2009), we can estimate the maximum relative velocity before disruption as function of the physical radii of the planetesimals. We found that the worst case scenario occurs for pairs with radii between 1 and 2 km, leading to disruption speeds higher than 70 m s^{-1}. Thus, it appears that both examples shown in Fig. 13 may in fact lead to constructive collisions and serve as breeding grounds for more massive embryos.

6 CONCLUSIONS

In this paper, we presented an algebraic map, dubbed MAMA, for the dynamical evolution of massless particles embedded in a gas disc, orbiting a central star and perturbed by a secondary stellar component with high eccentricity. Only coplanar motion is considered. The MAMA was constructed combining two models, one for the secular dynamics generated by the gravitational perturbations from the secondary star (Heppenheimer 1978; Thébault et al. 2006; Giuppone et al. 2011), plus a second set of equations modelling the effects of a non-lineal gas drag (Adachi et al. 1976; Weidenschilling et al. 1997; Supulver & Lin 2000; Beaugé et al. 2010).

The map was shown to be precise and able to reproduce the secular dynamics of small planetesimals in circumstellar orbits in
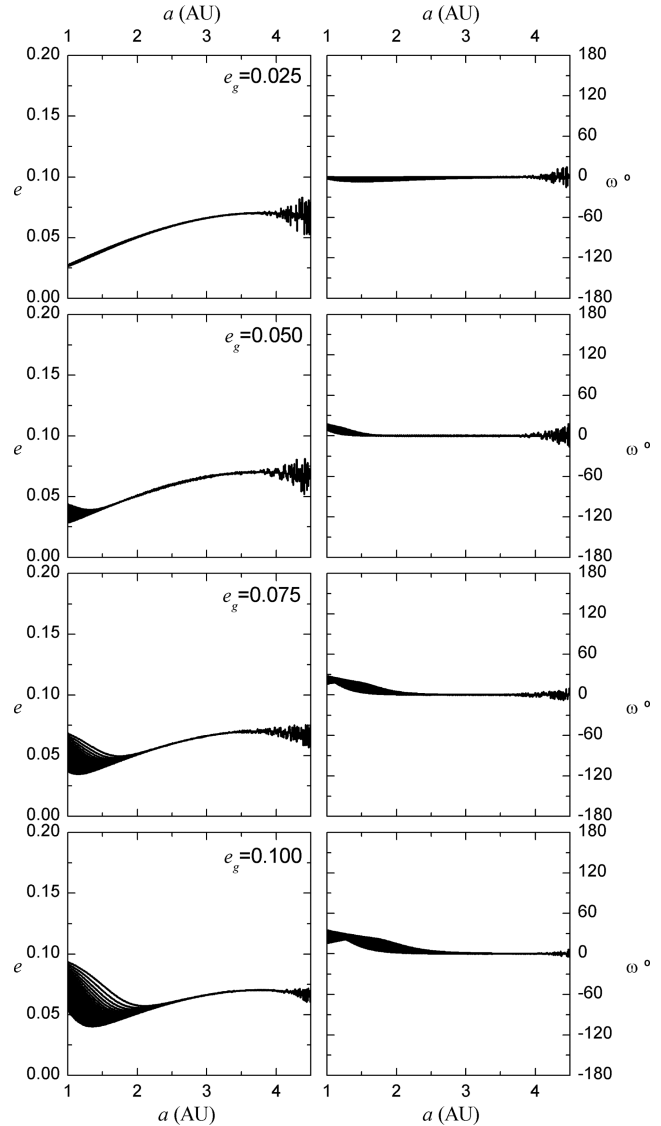

Figure 11. Eccentricity (left) and longitude of pericentre (right) for planetesimals with sizes between $1 \text{ km} \leq s \leq 10 \text{ km}$ ($\Delta s = 0.025 \text{ km}$) as function of the semimajor axis a. The graphs show the planetesimals after 3×10^5 yr, when all achieved their equilibrium solutions. For the simulation, we assume a static and aligned gas disc ($\omega = 0°$, $g_g = 0$) and we change its eccentricity: $e_g = 0.025$ (top panels), 0.05, 0.075 and 0.1 (bottom panels).

TBS. It is at least 100 times faster than conventional *N*-body codes, making it a good work bench with which to study possible scenarios for planetary accretion.

Although resonant interactions in the outer parts of the gas disc could invalidate the secular approximation, we found that capture can only occur for very small planetesimals. For all other bodies, or semimajor axis below $\sim$3 au, the secular model should be fairly precise.

As an example, we applied MAMA to the γ-Cephei system, a TBS with a giant exoplanet orbiting its main star at approximately 2 au. We analysed the evolution of 16 000 collisionless particles with sizes between 0.025 and 20 km, and distributed from 1 to 4 au. We considered an eccentric and static disc aligned with the orbit of the binary. The eccentricity of the disc was chosen as the test parameter, varying its magnitude between 0.025 and 0.2. For each
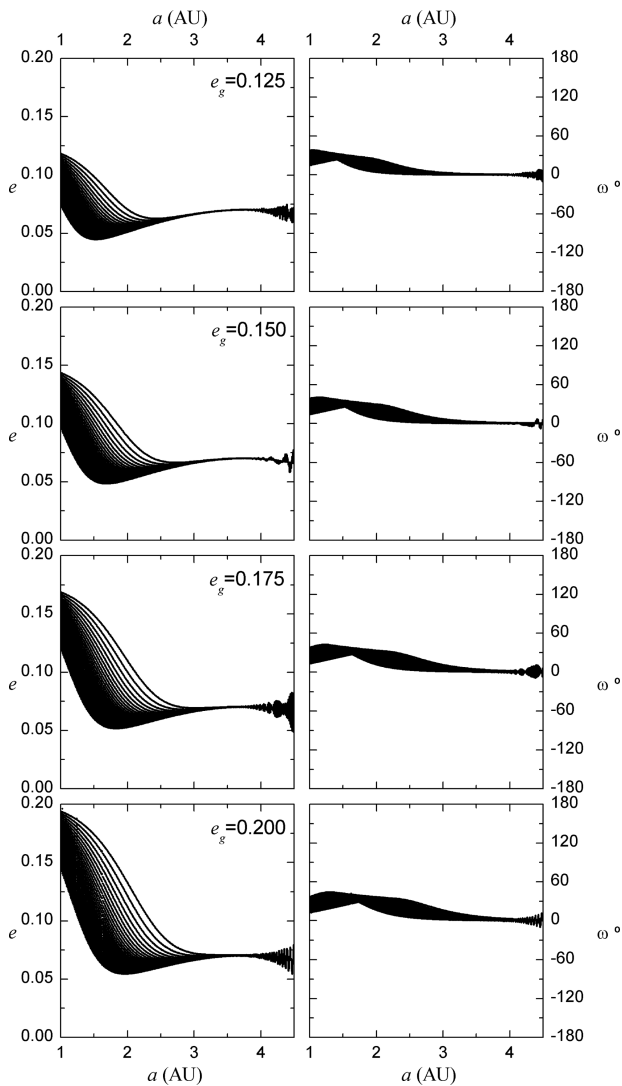
Figure 12. Eccentricity (left) and longitude of pericentre (right) for planetesimals with sizes between $1\,\text{km} \leq s \leq 10\,\text{km}$ ($\Delta s = 0.025\,\text{km}$) as function of the semimajor axis a. The graphs show the planetesimals after 3×10^5 yr, when all achieved their equilibrium solutions. For the simulation, we assume a static and aligned gas disc ($\omega = 0°$, $g_{\text{g}} = 0$) and we change its eccentricity: $e_{\text{g}} = 0.125$ (top panels), 0.15, 0.175 and 0.2 (bottom panels).
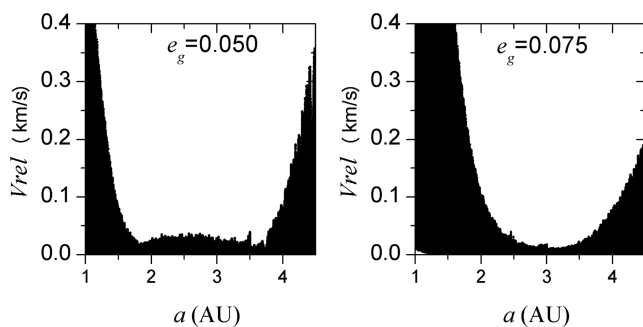

Figure 13. Distribution of relative velocities V_{rel} for planetesimals of different sizes ($1 \leq s \leq 10\,\text{km}$), in an aligned static gas disc with eccentricity $e_{\text{g}} = 0.05$ (left) and 0.075 (right). The impact speeds were calculated once the planetesimals achieved their equilibrium solutions. Both cases show a region where V_{rel} is below of the critical limit for disruption, here estimated to be $\sim 70\,\text{m s}^{-1}$ (Stewart & Leinhardt 2009).

value, we simulated the evolution of 16 000 particles for 3×10^5 yr, with low computational cost.

We were able to calculate the relative velocity between all the pairs of particles, and estimate their collisional dynamics. We found that a disc with $e_{\text{g}} = 0.05$ appears to define a relatively large region in the semimajor axis domain where impact velocities are sufficiently low to lead to accretion. This region contains the present location of the exoplanet.

Notwithstanding this encouraging result, the aim of this paper was not a detailed and extensive search for accretional scenarios in TBS, but to present a series of examples of possible applications. Future implementations will show whether this or other scenarios may hold the key to planetary formation in these complex systems.

ACKNOWLEDGEMENT

REFERENCES

Adachi I., Hayashi C., Nakazawa K., 1976, Prog. Theor. Phys., 56, 1756
Artymowicz P., Lubow S. H., 1994, ApJ, 421, 651
Beaugé C., Leiva A. M., Haghighipour N., Correa Otto J., 2010, MNRAS, 408, 503
Carpino M., Milani A., Nobili A. M., 1987, A&A, 147, 205
Chauvin G., Beust H., Lagrange A. M., Eggenberger A., 2011, A&A, 528, 8
Cincotta P. M., Simó C., 2000, A&AS, 147, 205
Cordeiro R. R., Canova A. L. F., Vieira Martins R., 1997, Celest. Mech. Dyn. Astron., 67, 215
Ferraz-Mello S., 1988, AJ, 96, 400
Giuppone C. A., Leiva A. M., Correa-Otto J., Beaugé C., 2011, A&A, 530, 103
Hatzes A. P., Cochran W. D., Endl M., McArthur B., Paulson D. B., Walker G. A. H., Campbell B., Yang S., 2003, ApJ, 599, 1383
Heppenheimer T. A., 1978, A&A, 65, 421
Kley W., 1999. MNRAS, 303, 696
Kley W., Nelson R. P., 2008, A&A, 486, 617
Kley W., Papaloizou J. C. B., Ogilvie G. I., 2008, A&A, 487, 671
Malhotra R., 1994, Celest. Mech. Dyn. Astron., 60, 373
Marzari F., Scholl H., 2000, ApJ, 543, 328
Marzari F., Scholl H., Thébault P., Baruteau C., 2009, A&A, 508, 1493
Marzari F., Baruteau C., Scholl H., Thébault P., 2012, A&A, 539, 98
Masset F., 2000, A&AS, 141, 165
Mikkola S., 1997, Celest. Mech. Dyn. Astron., 68, 249
Moons M., Morbidelli A., 1993. Celest. Mech. Dyn. Astron., 57, 99
Müller T. W. A., Kley W., 2012, A&A, 539, 18
Paardekooper S.-J., Leinhardt Z. M., 2010, MNRAS, 403, 64
Paardekooper S.-J., Thébault P., Mellema G., 2008, MNRAS, 386, 973
Rafikov R. R., 2013, ApJ, 765, L8
Roy A. E., 2005, Orbital Motion. IOP Publishing Ltd, Bristol
Stewart S. T., Leinhardt Z. M., 2009, ApJ, 691, 133
Supulver K. D., Lin D. N. C., 2000, Icarus, 146, 525
Thébault P., 2011, Celest. Mech. Dyn. Astron., 111, 29
Thébault P., Marzari F., Scholl H., Turrini D., Barbieri M., 2004, A&A, 427, 1097
Thébault P., Marzari F., Scholl H., 2006, Icarus, 183, 193
Weidenschilling S. J., Spaute D., Davis D. R., Marzari F., Ohtsuki K., 1997, Icarus, 128, 429

This paper has been typeset from a TeX/LaTeX file prepared by the author.